symmetry

MDPI

Article

Synthesis, Crystal Structure, Local Structure, and Magnetic Properties of Polycrystalline and Single-Crystalline $Ce_2Pt_6Al_{15}$

Kyugo Ota [1], Yuki Watabe [1], Yoshinori Haga [2], Fabio Iesari [3], Toshihiro Okajima [3] and Yuji Matsumoto [1,*]

[1] Graduate School of Science and Engineering, University of Toyama, Toyama 930-8555, Japan
[2] Advanced Science Research Center, Japan Atomic Energy Agency, Tokai 319-1195, Japan; haga.yoshinori@jaea.go.jp
[3] Aichi Synchrotron Radiation Center, Seto 489-0965, Japan; fabio.iesari@aichisr.jp (F.I.); toshihiro.okajima@aichisr.jp (T.O.)
* Correspondence: ymats@sci.u-toyama.ac.jp

Abstract: Asymmetry, such as non-centrosymmetry in the crystal or chiral structure and local symmetry breaking, plays an important role in the discovery of new phenomena. The honeycomb structure is an example of an asymmetric structure. $Ce_2Pt_6Al_{15}$ is a candidate for a frustrated system with honeycomb Ce-layers, which have been reported to show near the quantum critical point. However, the ground state of $Ce_2Pt_6Al_{15}$ depends on the sample, and analysis of the crystal structure is difficult due to the presence of stacking disorder. We synthesized polycrystalline $Ce_2Pt_6Al_{15}$ using arc melting method (AM-$Ce_2Pt_6Al_{15}$) and single-crystalline $Ce_2Pt_6Al_{15}$ using flux method (F-$Ce_2Pt_6Al_{15}$). The prepared samples were characterized by electron probe micro-analysis (EPMA), single and powder X-ray diffraction methods, measured magnetic properties and X-ray absorption spectroscopy (XAS). The composition ratio of AM-$Ce_2Pt_6Al_{15}$ was stoichiometric, although it contained a small amount (i.e., a few percent) of the impurity $Ce_2Pt_9Al_{16}$. Meanwhile, the composition ratio of F-$Ce_2Pt_6Al_{15}$ deviated from stoichiometry. The X-ray absorption fine structure (XAFS) spectrum of AM-$Ce_2Pt_6Al_{15}$ at the Ce L_3-edge was similar to that of CeF_3, which possesses the Ce^{3+} configuration, indicating that the valence of Ce in $Ce_2Pt_6Al_{15}$ is trivalent; this result is consistent with that for the magnetic susceptibility. To determine the precise structure, we analyzed the extended X-ray absorption fine structure (EXAFS) spectra of Ce L_3- and Pt L_3-edges for $Ce_2Pt_6Al_{15}$, and found that the EXAFS spectra of $Ce_2Pt_6Al_{15}$ can be explained not as a hexagonal $Sc_{0.6}Fe_2Si_{4.9}$-type structure but, instead, as an orthorhombic structure with honeycomb structure.

Keywords: single crystal X-ray diffraction; heavy fermion; X-ray absorption; $Ce_2Pt_6Al_{15}$; XAFS; EXAFS; honeycomb structure; $Sc_{0.6}Fe_2Si_{4.9}$-type structure

Citation: Ota, K.; Watabe, Y.; Haga, Y.; Iesari, F.; Okajima, T.; Matsumoto, Y. Synthesis, Crystal Structure, Local Structure, and Magnetic Properties of Polycrystalline and Single-Crystalline $Ce_2Pt_6Al_{15}$. *Symmetry* **2023**, *15*, 1488. https://doi.org/10.3390/sym15081488

Academic Editor: Alexey V. Lukoyanov

Received: 15 May 2023
Revised: 5 June 2023
Accepted: 9 June 2023
Published: 27 July 2023

1. Introduction

Many curious physical properties have been observed in strongly correlated *f* electron systems, such as non-Fermi liquid (NFL), unconventional quantum critical behavior, and so on. The magnetic frustration effect is one of the most important properties for anomalous phenomena. Quantum critical behavior due to the magnetic frustration effect in YbAgGe with the distorted kagome lattice has been observed [1]. In $YbRh_2Si_2$, unconventional quantum critical behavior has been observed [2,3], and the magnetic frustration effect was considered as a candidate for the origin of the critical behavior [4]. CePdAl with the distorted kagome lattice is a partially magnetically frustrated system: 2/3 of the Ce exhibits long-range order, while 1/3 does not participate in long-range magnetic ordering [5]. These properties have been observed around the quantum critical point with frustrated systems. Therefore, searching for compounds presenting magnetic frustration may facilitate the discovery of novel quantum phenomena.

One of the origins of this frustration is the geometric arrangement (e.g., a honeycomb lattice) of the atoms of interest. In the system with non-centrosymmetric crystal structure,

unconventional superconductivity has been observed [6]. Kitaev spin liquid [7] and current-induced magnetoelectric effects in a toroidal magnetic ordered state [8] have recently been observed in crystals possessing honeycomb structure.

The $R_2T_6X_{15}$ (R = rare earth and actinide, T = Pt, Pd, Fe, Ni, X = Al, Ga, Si) system is one of the candidates for determining frustrated systems with honeycomb structure. Several rare-earth and uranium compound series belonging to this system, such as R-Pd-X [9], R-Pt-X [10–25], R-Ni-(Ga, Ge) [26], and R-Fe-Si [27–29], have been reported. In the early stages of research, this crystal structure was solved as the hexagonal $Sc_{0.6}Fe_2Si_{4.9}$-type structure (space group 194 ($P6_3/mmc$)) [19], as shown in Figure 1a,c. This structure consists of R_2X_3- and TX_2-layers. The occupancies of R and X(1) sites in the R_2X_3-layer are 2/3 and 1/3, respectively, indicating that these sites are only partially occupied. The nearest R–R distance is about 4 Å. The distance between the R_2X_3-layer is about twice larger than the R–R distance, indicating that the magnetic interaction is two-dimensional. In the recent reports, superstructure reflections corresponding to a larger in-plane lattice parameters have been observed, suggesting the formation of a superstructure of the original hexagonal unit cell. Moreover, the existence of streak scattering along the [001]-direction indicates stacking disorder in the superstructure. Overall observations have led to the conclusion of the formation of R_2X_3 honeycomb layers with local orthorhombic symmetry (space group 63 ($Cmcm$)) [25], as shown in Figure 1b,d. Most of the research focused on this system has utilized the X-ray diffraction method; however, X-ray diffraction is not sensitive enough for analysis of the stacking disorder in the crystal structure. On the other hand, there has been only one report on the use of X-ray absorption fine structure (XAFS) for $Ce_2Pt_6Ga_{15}$ [19], which is much more sensitive to the local symmetry. Therefore, one of the purposes of this paper is to detail our XAFS measurements, which were made in order to clarify the local structure of $Ce_2Pt_6Ga_{15}$. In X-ray diffraction, only the averaged structure is observed. As the local structure is averaged over the stacking disorder, it cannot be used to distinguish whether the R and X sites in the R_2X_3-layer are randomly occupied or not.

There have been contradicting reports on the physical properties of $Ce_2Pt_6Al_{15}$. The polycrystalline $Ce_2Pt_6Al_{15}$ prepared by arc melting (AM-$Ce_2Pt_6Al_{15}$) was an antiferromagnet with T_N = 2.6 K [25], while $Ce_2Pt_6Al_{15}$ prepared by unknown method [30] and the single-crystalline [31] $Ce_2Pt_6Al_{15}$ prepared using flux method (F-$Ce_2Pt_6Al_{15}$) exhibited NFL behavior. As a possible origin of the sample dependence, the difference in the local crystal structure arising from different preparation methods was inferred. As such, a further purpose of this study is to clarify the crystallographic difference between AM- and F-$Ce_2Pt_6Al_{15}$ samples and to discuss the existing contradicting physical data by detailing the measured magnetic properties in well-characterized $Ce_2Pt_6Al_{15}$ samples.

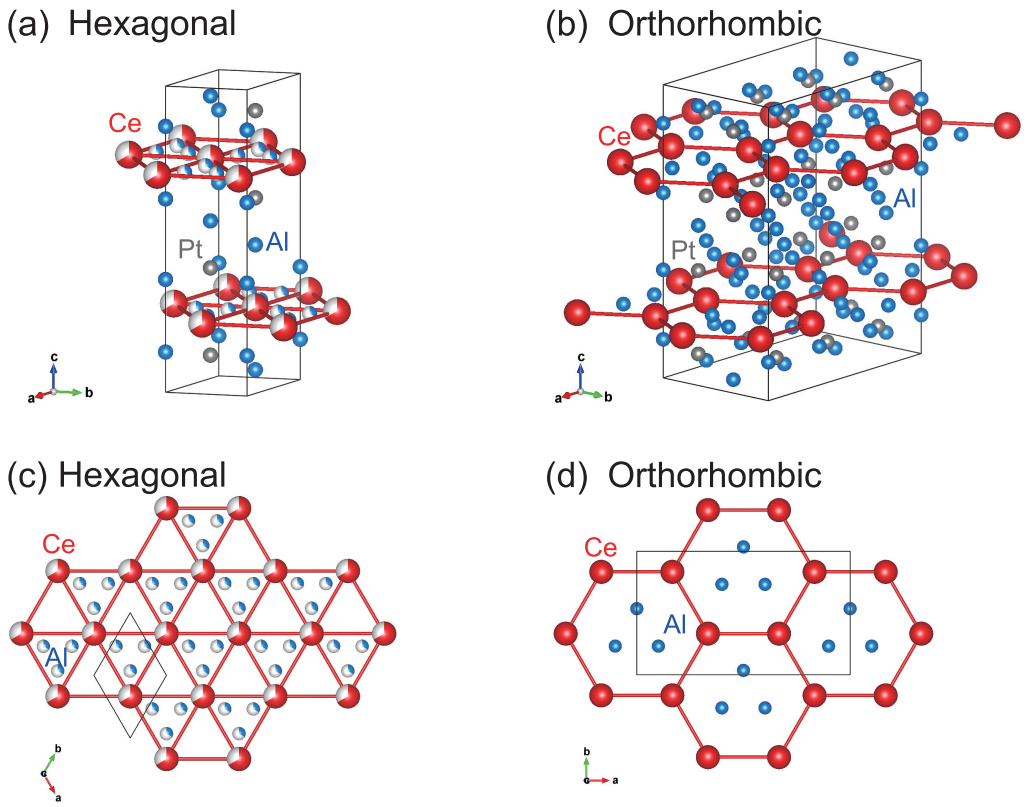

Figure 1. The crystal structure of $Ce_2Pt_6Al_{15}$ with (**a**) hexagonal structure (space group 194 ($P6_3/mmc$)) and (**b**) orthorhombic structure (space group 63 ($Cmcm$)). The Ce_2Al_3-layer of (**c**) hexagonal structure and (**d**) orthorhombic structure. The black lines in (**c**,**d**) indicate the unit cell. The occupancies of Ce and Al(1) sites in Ce_2Al_3-layer of hexagonal structure are 2/3 and 1/3, respectively, and the Ce atoms coordinate the triangular structure. The Ce atoms with orthorhombic structure coordinate the honeycomb structure.

2. Experimental

AM-$Ce_2Pt_6Al_{15}$ was prepared by arc melting method under Ar atmosphere. The purity of elements were 3N (99.9%):Ce, 3N:Pt, and 6N:Al. F-$Ce_2Pt_6Al_{15}$ was prepared by the aluminum self-flux method. Ce, Pt, and Al with the starting composition 1:3:30 were loaded in an alumina crucible and then sealed in a quartz tube under high vacuum. The sealed tube was heated to 1050 °C, soaked for 6 h, then cooled to 700 °C in 268 h. The excess Al was spun off in a centrifuge. Figure 2 shows a photograph of the F-$Ce_2Pt_6Al_{15}$.

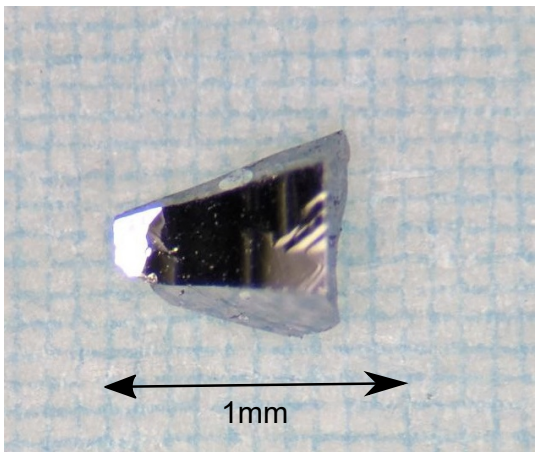

Figure 2. The photograph of F-$Ce_2Pt_6Al_{15}$.

Powder X-ray diffraction measurements were performed using Rint 2100 (Rigaku) using Cu Kα radiation at room temperature. The powder was prepared using a mortar. Rietveld analysis was performed using the Rietan-FP program [32].

Single crystal X-ray diffraction measurements were performed with R-AXIS RAPID (Rigaku) diffractometer using Mo Kα radiation at room temperature. Small pieces (~0.05 mm) for single crystal X-ray diffraction measurements were prepared by cutting the sample with a knife. The final atomic coordinates and occupancies were refined using the SHELXL97 program [33].

The compositions were determined by electron-probe micro analysis (EPMA; (JEOL JXA-8230) with CeP_5O_{14}, Pt, and Al as a reference materials at room temperature. Samples were polished using the emery papers to measure EPMA.

The magnetic properties were performed by a superconducting quantum interference device (SQUID) magnetometer (Quantum Design MPMS) from 330 to 2 K under a magnetic field up to 7 T.

XAFS measurements were performed using the BL11S2 at the Aichi Synchrotron Radiation Center in transmission geometry at the Ce L-edge (L_3 : 5723 eV) and Pt L-edge (L_3 : 11,563 eV) at room temperature. CeF_3 and CeO_2 were used as reference compounds for Ce^{3+} and Ce^{4+} valency, respectively. The XAFS spectra were processed and analyzed using ATHENA and ARTEMIS codes [34].

The extended X-ray absorption fine structure (EXAFS) analyses were performed using the following equation,

$$\chi(k) = S_0^2 \sum_j \frac{N_j F_j(k)}{kR_j^2} \sin(2kR_j + \delta_j(k)) e^{-2(\sigma_j^2 k^2 + \frac{R_j}{\lambda(k)})} \quad (1)$$

where χ denotes the EXAFS oscillation; k is the wavenumber of the photoelectron; S_0^2 is the probability of single-electron excitation; N_j, R_j, $F_j(k)$, σ_j^2, and $\delta_j(k)$ are the co-ordination number, inter-atomic distance, back-scattering atomic form factor, Debye–Waller factor, and phase shift of the neighboring atom j, respectively; and $\lambda(k)$ is the mean free path of photoelectrons.

3. Results and Discussion

3.1. EPMA

The compositions of the AM- and F-$Ce_2Pt_6Al_{15}$ samples were analyzed by EPMA. Figure 3 shows the back-scattered electron (BSE) images and the counter map images of Ce, Pt, and Al in AM-$Ce_2Pt_6Al_{15}$. The few black points and lines in the BSE images are scratches that occurred during polishing. A clear gradation can be observed in the BSE images, indicating that the sample possessed two phases. The compositions of Ce, Pt, and Al of the bright area (phase 1) in the BSE image differ from those in the gray area (phase 2). We identified phase 1 as the impurity $Ce_2Pt_9Al_{16}$ phase and phase 2 as $Ce_2Pt_6Al_{15}$. The composition ratio of AM-$Ce_2Pt_6Al_{15}$ (phase 2) was Ce:Pt:Al = 2.11(6):6:15.5(4).

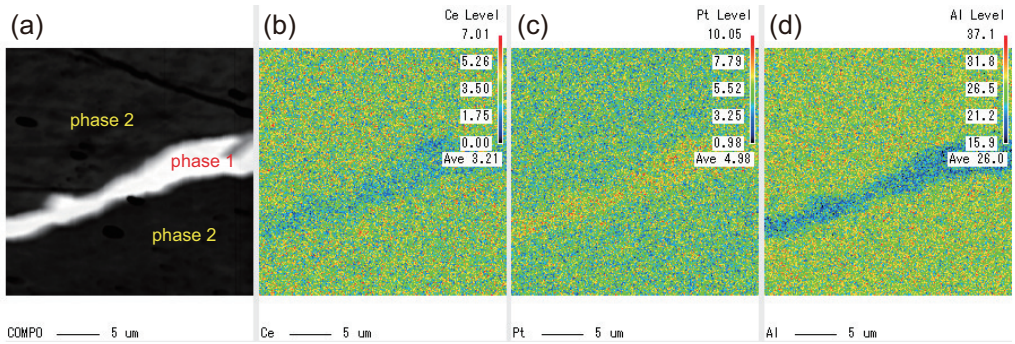

Figure 3. (**a**) The backscattered electron (BSE) images, the counter map images of (**b**) Ce, (**c**) Pt, and (**d**) Al of AM-$Ce_2Pt_6Al_{15}$. Phase 1 is impurity $Ce_2Pt_9Al_{16}$ phase and phase 2 is $Ce_2Pt_6Al_{15}$ phase.

There is no impurity phase in F-$Ce_2Pt_6Al_{15}$. The composition ratio of F-$Ce_2Pt_6Al_{15}$ was Ce:Pt:Al = 2.09(8):6:16.5(3), indicating that the ratio of Al in the F-$Ce_2Pt_6Al_{15}$ is rich.

3.2. Powder X-ray Diffraction

We conducted powder X-ray diffraction on AM- and F-$Ce_2Pt_6Al_{15}$ samples. Figure 4a shows the Rietveld plot of AM-$Ce_2Pt_6Al_{15}$. The reliability factor-weighted pattern R_{wp} and Goodness of fit S were 16.842 and 1.4555, respectively. Most of the Bragg peaks were assigned according to the hexagonal $Sc_{0.6}Fe_2Si_{4.9}$-type structure (space group 194 ($P6_3/mmc$), and we determined that the lattice constants a and c were 4.3082(3) Å and 16.5040(10) Å, respectively. The powder X-ray diffraction showed weak impurity peaks, indicating the existence of a few impurity phases in the sample. These peaks were assigned to $Ce_2Pt_9Al_{16}$ with orthorhombic $Ce_2Pt_9Al_{16}$-type structure [35,36]. The impurity was also detected in the EPMA measurements.

Figure 4b shows the Rietveld plot of F-$Ce_2Pt_6Al_{15}$. The R_{wp} and S values were 21.742 and 1.5068, respectively. Most of diffraction patterns were indexed by the hexagonal $Sc_{0.6}Fe_2Si_{4.9}$-type structure, and we determined that the lattice constants a and c were 4.3207(3) Å and 16.4776(8) Å, respectively. A small peak from Al was detected; this impurity is likely to be the flux that could not be removed by the centrifuge.

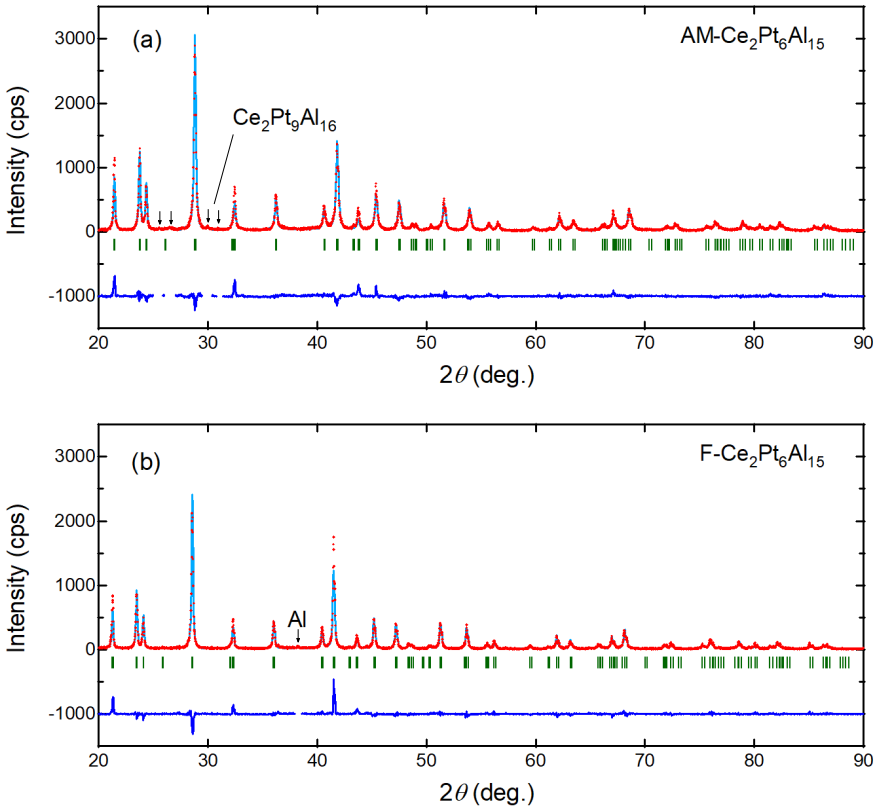

Figure 4. The Rietveld plot of (**a**) AM-$Ce_2Pt_6Al_{15}$ and (**b**) F-$Ce_2Pt_6Al_{15}$ analyzed by RIETAN-FP [32]. The red dots indicate experimental data. The solid light blue line indicates calculated diffraction patterns. The vertical bars indicate calculated peak positions for $Ce_2Pt_6Al_{15}$. The blue line indicates the residual error. The arrows indicate the impurity phase of (**a**) $Ce_2Pt_9Al_{16}$ and (**b**) Al. 2θ around the impurity peaks were not used for Rietveld analysis.

3.3. Single Crystal X-ray Diffraction

We performed single crystal X-ray diffraction measurements of AM- and F-$Ce_2Pt_6Al_{15}$. For this, we analyzed the crystal structure using hexagonal $Sc_{0.6}Fe_2Si_{4.9}$-type structure, which is the averaged structure of the orthorhombic ordered structure, as it is difficult to analyze

the effect of stacking defects. Crystallographic data, structure refinements, fractional co-ordinates, occupancy, and equivalent atomic displacement parameters U_{eq} for $Ce_2Pt_6Al_{15}$ are given in Tables 1 and 2. The lattice parameters of AM-$Ce_2Pt_6Al_{15}$ were a = 4.3127(7) Å and c = 16.5156(13) Å, and those for F-$Ce_2Pt_6Al_{15}$ were a = 4.3322(4) Å and c = 16.4976(7) Å, indicating that the uniaxial chemical pressure effect between AM-$Ce_2Pt_6Al_{15}$ and F-$Ce_2Pt_6Al_{15}$ can be expected. We fitted the site occupancies assuming the occupancy of Pt as 100%. The occupancies of Ce and Al sites of AM-$Ce_2Pt_6Al_{15}$ were close to the stoichiometric ratios. On the other hand, the occupancies of Al sites in F-$Ce_2Pt_6Al_{15}$ deviated from the stoichiometric ratio; namely, the composition ratio of Al in the F-$Ce_2Pt_6Al_{15}$ is rich. The composition ratios estimated according to the results of the single crystal X-ray diffraction experiments were consistent with those of EPMA.

Table 1. Crystallographic data and structure refinements for AM- and F-$Ce_2Pt_6Al_{15}$ analyzed by hexagonal $Sc_{0.6}Fe_2Si_{4.9}$-type structure.

	AM-$Ce_2Pt_6Al_{15}$	**F-$Ce_2Pt_6Al_{15}$**
Space group	194	194
Lattice constants (Å)	a = 4.3127(7) c = 16.5156(13)	a = 4.3322(4) c = 16.4976(7)
Formula units per cell, Z	1	1
Formula mass	1855.50	1855.50
Calculated density (g cm^{-3})	11.581	11.490
Absorption coefficient μ (mm^{-1})	87.809	87.114
Detector distance (mm)	127.40	127.40
θ range (deg.)	2.46–34.88	2.47–34.89
Range in hkl	$-6 \leq h \leq 6$ $-5 \leq k \leq 6$ $-26 \leq l \leq 25$	$-5 \leq h \leq 6$ $-6 \leq k \leq 6$ $-26 \leq l \leq 25$
Total number of reflections	3596	5905
Unique reflections	266	267
Reliability factor R_{int}	0.0258	0.0522
Goodness-of-fit	1.177	1.259
Reflections with $I > 2\sigma(I)$	243	253
Number of variables	21	21
R_1	0.0109	0.0111
wR_2	0.0146	0.0208
Residual electron density ($\Delta\rho_{max}/\Delta\rho_{min}$ e Å^{-3})	0.73/−1.15	0.78/−0.94

We converted the lattice parameters from the hexagonal $Sc_{0.6}Fe_2Si_{4.9}$-type structure to an orthorhombic ordered model (space group 63 (*Cmcm*)) to analyze the EXAFS according to the orthorhombic model; the results are shown in Table 3. We obtained the inter-atomic distance and co-ordination number (N) of neighboring atoms around Ce, Pt(1), and Pt(2) sites, which are given in Table 4. EXAFS analysis was performed using these parameters as initial conditions. Figure 5 shows the Ce, Pt, and Al sites with their surrounding neighboring atoms.

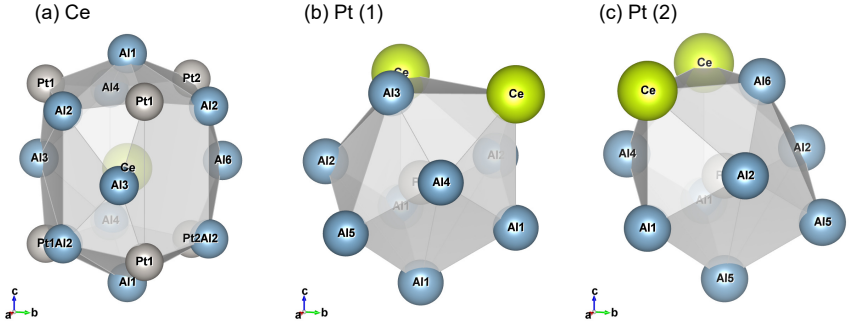

Figure 5. Near neighbor atoms in the orthorhombic structure of $Ce_2Pt_6Al_{15}$: Ce (**a**), Pt(1) (**b**), and Pt(2) (**c**).

Table 2. Fractional coordinates, occupancy, and equivalent atomic displacement parameters U_{eq} of AM- and F-$Ce_2Pt_6Al_{15}$ analyzed by hexagonal $Sc_{0.6}Fe_2Si_{4.9}$-type structure.

AM-$Ce_2Pt_6Al_{15}$					
Atom	***x***	***y***	***z***	**Occupancy**	**U_{eq} (Å^2)**
Ce	1/3	2/3	1/4	0.6715(17)	0.00514(13)
Pt	1/3	2/3	0.60755(2)	1	0.00495(5)
Al(1)	0.5354(4)	0.0709(7)	1/4	0.337(5)	0.0064(8)
Al(2)	0	0	0.13147(7)	1.008(6)	0.0078(4)
Al(3)	1/3	2/3	0.04594(7)	0.993(7)	0.0061(4)
F-$Ce_2Pt_6Al_{15}$					
Atom	***x***	***y***	***z***	**Occupancy**	**U_{eq} (Å^2)**
Ce	1/3	2/3	1/4	0.6777(19)	0.00603(14)
Pt	1/3	2/3	0.60727(2)	1	0.00598(6)
Al(1)	0.5349(4)	0.0699(8)	1/4	0.343(5)	0.0092(8)
Al(2)	0	0	0.13227(7)	1.065(6)	0.0098(3)
Al(3)	1/3	2/3	0.04672(7)	1.074(7)	0.0091(4)

Table 3. Atomic parameters of $Ce_2Pt_6Al_{15}$ for orthorhombic structure model. The lattice parameters are a = 12.9381 Å, b = 7.4698 Å, and c = 16.5156 Å.

Atom	***x***	***y***	***z***
Ce	1/6	1/6	1/4
Pt(1)	1/3	1/3	0.1076
Pt(2)	0	1/3	0.1076
Al(1)	1/6	1/6	0.0459
Al(2)	1/3	0	0.1315
Al(3)	0.3990	0.2678	1/4
Al(4)	0	0	0.1315
Al(5)	0	1/3	0.5459
Al(6)	0	0.4646	1/4

Table 4. Interatomic distance and coordination number (N) of neighboring atoms around Ce, Pt(1), and Pt(2) sites for $Ce_2Pt_6Al_{15}$ of orthorhombic model below 4 Å.

Ce			**Pt(1)**			**Pt(2)**		
Site	**Distance (Å)**	***N***	**Site**	**Distance (Å)**	***N***	**Site**	**Distance (Å)**	***N***
Al(3)	3.098	1	Al(2)	2.521	2	Al(4)	2.521	1
Al(6)	3.099	1	Al(4)	2.521	1	Al(2)	2.521	2
Al(3)	3.099	1	Al(1)	2.535	1	Al(5)	2.535	1
Al(2)	3.167	4	Al(3)	2.549	1	Al(6)	2.549	1
Al(4)	3.167	2	Al(1)	2.690	2	Al(1)	2.690	2
Al(1)	3.370	2	Al(5)	2.690	1	Al(5)	2.690	1
Pt(1)	3.426	4	Ce	3.426	2	Ce	3.426	2
Pt(2)	3.426	2						

3.4. X-ray Absorption Spectroscopy

Figure 6 shows the Ce L_3-edge XAFS spectra of AM-$Ce_2Pt_6Al_{15}$, CeF_3, and CeO_2. CeF_3 and CeO_2 were used as reference compounds for trivalent and tetravalent Ce, respectively. A peak structure was observed around 5720 eV, which corresponds to the Ce L_3-edge. In all the spectra, a clear oscillation structure was observed above L_3-edge. The XAFS edge energy of $Ce_2Pt_6Al_{15}$ was close to that of trivalent reference CeF_3, while the edge energy of tetravalent CeO_2 had a higher value, as expected, given that edge energy increases as the oxidation state of the absorber increases. Thus, the Ce valence in $Ce_2Pt_6Al_{15}$ was determined to be trivalent and Ce should possess the local magnetic moment. The peak of $Ce_2Pt_6Al_{15}$ was broader than that of CeF_3, implying that this system may be in a mixed valency state.

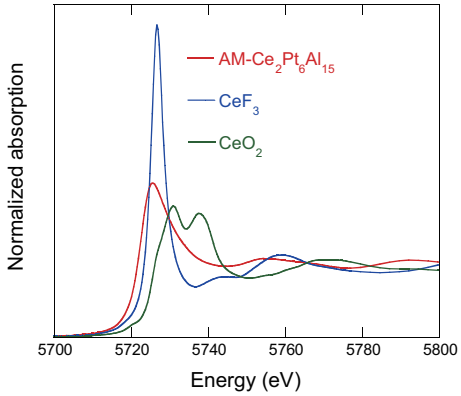

Figure 6. Normalized XAFS spectra of Ce L_3-edge of AM-$Ce_2Pt_6Al_{15}$, CeF_3, and CeO_2.

We analyzed the EXAFS spectra for AM-$Ce_2Pt_6Al_{15}$ around the Ce and Pt sites considering the orthorhombic structure. Although there was a slight difference, the Pt(1) and Pt(2) sites had almost identical local structure and, therefore, we assume that their contributions to the spectra were identical. Figures 7a and 8a show the XAFS spectra of Ce and Pt sites. In the process of structural refinement, the data in the range of 1.57–4.00 Å for Ce, and 1.23–3.49 Å for Pt was considered as indicated by a blue line in Figures 7c and 8c. By analyzing the spectra with respect to the Ce site, 9 first neighbor atoms located around 3.1 Å (Al(2), Al(3), Al(4) and Al6)) and 6 second neighbor atoms located around 3.4 Å (Pt(1) and Pt(2)) were identified. On the other hand, the hexagonal $Sc_{0.6}Fe_2Si_{4.9}$-type structure model predicts the existence of Al atoms around Ce within a very short distance (i.e., 1.5 A). However, the corresponding peak structure was not observed in the XAFS spectra, indicating the plausibility of the orthorhombic structure.

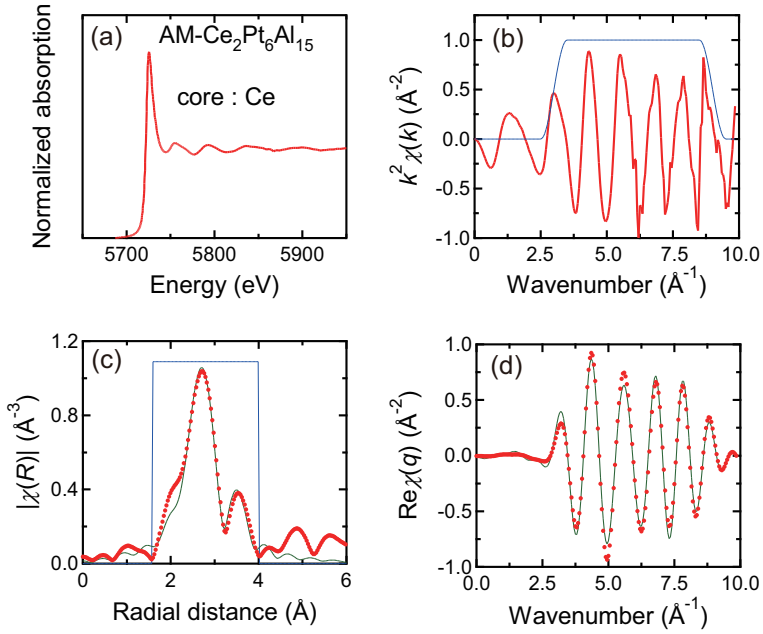

Figure 7. (**a**) Ce L_3-edge XAFS spectra of AM-$Ce_2Pt_6Al_{15}$, (**b**) k^2-weighted Ce L_3-edge $\chi(k)$ spectra of AM-$Ce_2Pt_6Al_{15}$, (**c**) corresponding $\chi(k)$ spectrum of AM-$Ce_2Pt_6Al_{15}$, and (**d**) inverse FTs of the $\chi(R)$ spectrum. The fits of $\chi(R)$ and Re($\chi(q)$) spectra using orthorhombic model are shown by green lines in (**c**,**d**). The k range used in the FTs was 3–9 $Å^{-1}$, as indicated by a blue line in (**b**). The R range used in the inverse FTs was 1.57–4 Å, as indicated by a blue line in (**c**).

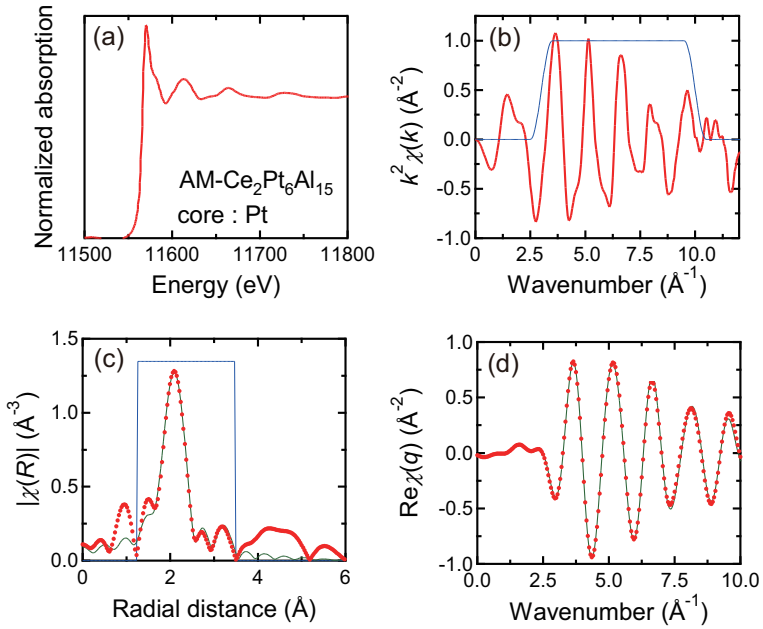

Figure 8. (**a**) Pt L_3-edge XAFS spectra of AM-$Ce_2Pt_6Al_{15}$: Pt(1), (**b**) k^2-weighted Pt L_3-edge $\chi(k)$ spectra of AM-$Ce_2Pt_6Al_{15}$: Pt(1), (**c**) corresponding $\chi(k)$ spectrum of AM-$Ce_2Pt_6Al_{15}$: Pt(1), and (**d**) inverse FTs of the $\chi(R)$ spectrum. The fits of $\chi(R)$ and Re($\chi(q)$) of $Ce_2Pt_6Al_{15}$: Pt(1) spectra using orthorhombic model are shown by green lines in (**c**,**d**). The k range used in the FTs was 3–10 Å^{-1}, as indicated by a blue line in (**b**). The R range used in the inverse FTs was 1.23–3.49 Å, as indicated by a blue line in (**c**).

We did not consider the scattering term between Ce and Al(1) site in the EXAFS analysis, as the corresponding intensity was expected to be weak. The first, second, and third neighbor atoms around the Pt site were 5 atoms around 2.5 Å (Al(1), Al(2), Al(3), and Al(4)), 3 atoms around 2.7 Å (Al(1) and Al(5)), and 2 atoms around 3.4 Å (Ce), respectively. The co-ordination numbers were kept fixed. The green lines in Figures 7d and 8d are the results of the structural refinement fit with the inverse Fourier transforms (FTs) of the experimental $\chi(R)$ spectra. The refined structural parameters are listed in Table 5, where N denotes the number of neighboring atoms, σ^2 is the Debye–Waller factor, and R is the inter-atomic distance between Ce or Pt and the neighboring scatter atoms. The experimental $\chi(R)$ spectra in Figures 7c and 8c are well-explained by the $\chi(R)$ spectra for Ce and Pt sites calculated using the orthorhombic model, indicating that $Ce_2Pt_6Al_{15}$ has a honeycomb structure.

Table 5. The refined structural parameters for AM-$Ce_2Pt_6Al_{15}$, where N is the number of neighboring atoms, σ^2 is the Debye-Waller factor, and R is interatomic distances between Ce or Pt sites and the neighboring scatter atoms.

	Neighbor	***N***	**σ^2 (Å^2)**	***R* (Å)**
Ce L_3-edge	1st: Al	9	0.012	3.12
	2nd: Pt	6	0.003	3.41
Pt L_3-edge	1st: Al	5	0.005	2.54
	2nd: Al	3	0.013	2.71
	3rd: Ce	2	0.011	3.40

3.5. Magnetic Properties

Figure 9a shows the temperature dependence of the magnetic susceptibility of AM- and F-$Ce_2Pt_6Al_{15}$. The susceptibility of AM-$Ce_2Pt_6Al_{15}$ at 0.1 T monotonously increased with decreasing temperature, corresponding to its paramagnetic behavior at high temperature, and it presented a broad maximum around 50 K. A broad maximum of susceptibility is often observed in heavy fermion systems, such as $CeRu_2Si_2$ [37], $Yb_2Pt_6Al_{15}$ [17], $YbPd_2Si_2$ [38,39], and so on.

Below 20 K, the magnetic susceptibility increases with paramagnetic behavior again. It has an antiferromagnetic-like anomaly at T^* = 2.6 K. These susceptibility behaviors are similar to those described by Radzieowski et al. [25]. According to the powder X-ray diffraction and EPMA measurements, this sample contained $Ce_2Pt_9Al_{16}$; notably, the T^* value was in good agreement with T_N = 2.6 K obtained previously for $Ce_2Pt_9Al_{16}$ [35,36]. The inset of Figure 9 shows the temperature dependence of the susceptibility of AM-$Ce_2Pt_6Al_{15}$ at low temperatures when magnetic fields are applied ($\mu_0 H$ = 0.1, 0.5, 1, 1.2, and 1.5 T). T^* shifted to lower temperatures with increasing magnetic field and disappeared above 1.5 T. The magnetic field dependence of T^* showed the same behavior as that observed by Strydom for $Ce_2Pt_9Al_{16}$, which vanished around $\mu_0 H$ = 1.5 T [36]. The anomaly at T^* and the paramagnetic behavior below 20 K are not likely to be intrinsic properties and the ground state of AM-$Ce_2Pt_6Al_{15}$ is non-magnetic. We also estimated the impurity from the magnetic susceptibility. The susceptibility increased with decreasing temperature below 20 K, and we assumed that the increase in magnetic susceptibility below 20 K was due to the presence $Ce_2Pt_9Al_{16}$. From this, we estimated that the impurity was 2–3% in the molar ratio.

Figure 9b indicates the inverse magnetic susceptibility of AM-$Ce_2Pt_6Al_{15}$ at $\mu_0 H$ = 0.1 T. At high temperature, it linearly increased with temperature, indicating that it follows the Curie–Weiss law. We fit the inverse susceptibility above 210 K using $\chi = C/(T - \theta_P)$ with the effective magnetic moment μ_{eff} and the Weiss temperature θ_P of 2.67 μ_B and −132 K, respectively. These values were similar to those obtained by Radzieowski et al. [25]. The observed μ_{eff} was close to the value of the Hund's Rule expected for Ce^{3+}, 2.54 μ_B, indicating that the $Ce_2Pt_6Al_{15}$ presents a magnetic moment derived from the $4f$ electrons of Ce at high temperature.

The magnetic susceptibility of F-$Ce_2Pt_6Al_{15}$ at 1 T monotonously increased with decreasing temperature, down to 2 K. It is possible that the ground state is NFL or magnetic order, as described by Manni et al. [30] and Suzuki et al. [31]. We fit the inverse susceptibility of F-$Ce_2Pt_6Al_{15}$ above 210 K using the Curie–Weiss law and obtained μ_{eff} and θ_P values of 2.90 μ_B and −17.4 K, respectively. The susceptibility behavior was quite different from that of AM-$Ce_2Pt_6Al_{15}$; this difference may have been caused by the difference in uniaxial effect and the deviation from stoichiometry between AM- and F-$Ce_2Pt_6Al_{15}$.

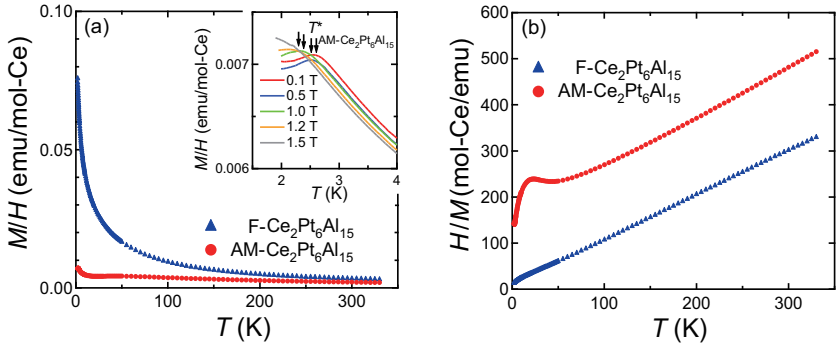

Figure 9. (**a**) The temperature dependence of the magnetic susceptibility of AM- and F-$Ce_2Pt_6Al_{15}$. The inset shows the temperature dependence of the susceptibility of AM-$Ce_2Pt_6Al_{15}$ at low temperature when magnetic fields are applied $\mu_0 H$ = 0.1, 0.5, 1, 1.2, and 1.5 T. The arrows indicate the T^*. (**b**) The temperature dependence of the inverse magnetic susceptibility of AM- and F-$Ce_2Pt_6Al_{15}$.

4. Conclusions

We synthesized AM-$Ce_2Pt_6Al_{15}$ using arc melting method and F-$Ce_2Pt_6Al_{15}$ using the Al-flux method. From the powder X-ray diffraction and EPMA results, the AM-$Ce_2Pt_6Al_{15}$ sample contained a $Ce_2Pt_9Al_{16}$ impurity, while there was no impurity phase in the F-$Ce_2Pt_6Al_{15}$. Crystal structure analysis through the powder and single crystal X-ray diffraction methods was performed according to the hexagonal $Sc_{0.6}Fe_2Si_{4.9}$-type structure (space group 194 ($P6_3/mmc$)). From the single crystal X-ray diffraction method, the lattice parameters of AM-$Ce_2Pt_6Al_{15}$ were a = 4.3127(7) Å and c = 16.5156(13) Å, while those

of F-$Ce_2Pt_6Al_{15}$ were a = 4.3322(4) Å and c = 16.4976(7) Å, indicating that the uniaxial chemical pressure effect between AM-$Ce_2Pt_6Al_{15}$ and F-$Ce_2Pt_6Al_{15}$ can be expected.

We performed XAS measurements of the AM-$Ce_2Pt_6Al_{15}$ sample. The magnetic properties of the Ce L_3-edge for the XAFS spectra of $Ce_2Pt_6Al_{15}$ were similar to those of CeF_3 which possesses Ce^{3+}, indicating that the valence state in $Ce_2Pt_6Al_{15}$ is trivalent. We analyzed the EXAFS spectra of Ce L_3- and Pt L_3-edges for $Ce_2Pt_6Al_{15}$, and found that the EXAFS spectra of $Ce_2Pt_6Al_{15}$ cannot be explained by the hexagonal $Sc_{0.6}Fe_2Si_{4.9}$-type structure. As such, the orthorhombic structure with honeycomb structure (space group 63 (*Cmcm*)) is plausible.

We measured the magnetic susceptibility of the AM- and F-$Ce_2Pt_6Al_{15}$ samples. Paramagnetic behavior was exhibited at high temperature, while antiferromagnetic-like order was observed at T^* = 2.6 K in AM-$Ce_2Pt_6Al_{15}$. These susceptibility behaviors are similar to those described by Radzieowski et al. [25]. The anomaly at T^* is likely to be caused by the impurity $Ce_2Pt_9Al_{16}$ and the non-magnetic ground state of AM-$Ce_2Pt_6Al_{15}$. The susceptibility behavior of F-$Ce_2Pt_6Al_{15}$ was quite different from that of AM-$Ce_2Pt_6Al_{15}$. This difference may be due to the difference in the uniaxial effect and the deviation from stoichiometry between AM-$Ce_2Pt_6Al_{15}$ and F-$Ce_2Pt_6Al_{15}$.

Author Contributions: Conceptualization, K.O. and Y.M.; validation, Y.W., Y.H. and F.I.; formal analysis, K.O., Y.W., Y.H., F.I. and Y.M.; investigation, K.O., Y.H. and Y.M.; resources, Y.H., T.O. and Y.M.; data curation, K.O., Y.W., Y.H., F.I. and Y.M.; writing—original draft preparation, K.O. and Y.M.; writing—review and editing, Y.W., Y.H., F.I. and T.O.; visualization, K.O. and Y.M.; supervision, Y.M.; project administration, Y.M.; funding acquisition, T.O. and Y.M. All authors have read and agreed to the published version of the manuscript.

Funding: This work was supported by the CREST (JPMJCR1861) from the Japan Science and Technology Agency (JST) and a Grant-in-Aid for Scientific Research (C) (No. 20K03857) from the Ministry of Education, Culture, Sports, Science and Technology, Japan.

Data Availability Statement: The data presented in this study are available from the corresponding author upon reasonable request.

Acknowledgments: We thank K. Tsuge for technical and analysis support of the single crystal X-ray diffraction measurement and we thank S. Yamada for technical support of EPMA. The XAFS measurements were conducted at the BL11S2 of Aichi Synchrotron Radiation Center (Proposal No. 202105059).

Conflicts of Interest: The authors declare no conflict of interest.

Abbreviations

The following abbreviations are used in this manuscript:

EPMA	electron micro-probe analysis
XAS	X-ray absorption spectroscopy
XAFS	X-ray absorption fine structure
EXAFS	extended X-ray absorption fine structure
NFL	non Fermi liquid
BSE	backscattered electron
FT	Fourier transform
AM-$Ce_2Pt_6Al_{15}$	$Ce_2Pt_6Al_{15}$ prepared by arc melting method
F-$Ce_2Pt_6Al_{15}$	$Ce_2Pt_6Al_{15}$ prepared by Al-flux method

References

1. Bud'ko, S.L.; Morosan, E.; Canfield, P.C. Magnetic field induced non-Fermi-liquid behavior in YbAgGe single crystals. *Phys. Rev. B* **2004**, *69*, 014415. [CrossRef]
2. Gegenwart, P.; Custers, J.; Geibel, C.; Neumaier, K.; Tayama, T.; Tenya, K.; Trovarelli, O.; Steglich, F. Magnetic-Field Induced Quantum Critical Point in $YbRh_2Si_2$. *Phys. Rev. Lett.* **2002**, *89*, 056402. [CrossRef] [PubMed]
3. Custers, J.; Gegenwart, P.; Wilhelm, H.; Neumaier, K.; Tokiwa, Y.; Trovarelli, O.; Geibel, C.; Steglich, F.; Pépin, C.; Coleman, P. The break-up of heavy electrons at a quantum critical point. *Nature* **2003**, *424*, 524–527. [CrossRef] [PubMed]

4. Si, Q.; Rabello, S.; Ingersent, K.; Smith, J.L. Locally critical quantum phase transitions in strongly correlated metals. *Nature* **2001**, *413*, 804–808. [CrossRef] [PubMed]
5. Dönni,A.; Ehlers, G.; Maletta, H.; Fischer, P.; Kitazawa, H.; Zolliker, M. Geometrically frustrated magnetic structures of the heavy-fermion compound CePdAl studied by powder neutron diffraction. *J. Phys. Condens. Matter* **1996**, *8*, 11213–11230. [CrossRef]
6. Kimura, N.; Ito, K.; Saitoh, K.; Umeda, Y.; Aoki, H.; Terashima, T. Pressure-induced superconductivity in noncentrosymmetric heavy-fermion $CeRhSi_3$. *Phys. Rev. Lett.* **2005**, *95*, 247004. [CrossRef]
7. Kasahara, Y.; Sugii, K.; Ohnishi, T.; Shimozawa, M.; Yamashita, M.; Kurita, N.; Tanaka, H.; Nasu, J.; Motome, Y.; Shibaushi, T.; et al. Unusual thermal Hall effect in a Kitaev spin liquid candidate α-$RuCl_3$. *Phys. Rev. Lett.* **2018**, *120*, 217205. [CrossRef]
8. Saito, H.; Uenishi, K.; Miura, N.; Tabata, C.; Hidaka, H.; Yanagisawa, T.; Amitsuka, H. Evidence of a new current-induced magnetoelectric effect in a toroidal magnetic ordered state of UNi_4B. *J. Phys. Soc. Jpn.* **2018**, *87*, 033702. [CrossRef]
9. Lutsyshyn, Y.; Tokaychuk, Y.; Gladyshevskii, R. Ternary compounds with $Sc_{0.6}Fe_2Si_{4.9}$-type structure in the systems Sm–{Pd, Pt}–Al. *Chem. Met. Alloys* **2012**, *5*, 98–102. [CrossRef]
10. Lutsyshyn, Y.; Tokaychuk, Y.; Gladyshevskii, R. Crystal structure of the compound $Tb_{0.67}Pt_2Al_5$. *Chem. Met. Alloys* **2009**, *2*, 75–82. [CrossRef]
11. Rousuli, A.; Nakamura, S.; Sato, H.; Ueda, T.; Matsumoto, Y.; Ohara, S.; Schwier, E.F.; Nagasaki, T.; Mimura, K.; Anzai, H.; et al. Photoemission study of the electronic structure of the Kondo lattices $Yb_2Pt_6X_{15}$ (X = Al, Ga). *Phys. Rev. B* **2017**, *96*, 045117. [CrossRef]
12. Prots, Y.; Deppe, M.; Cardoso-Gil, R.; Cervellino, A.; Ormeci, A.; Geibel, C.; Grin, Y. $Yb_2Al_{15}Pt_6$—The most ordered variety of the $Sc_{1.2}Fe_4Si_{9.8}$ aristotype. *Chem. Met. Alloys* **2014**, *7*, 85–99. [CrossRef]
13. Niermann, J.; Jeitschko, W. Ternary Aluminides with the Ideal Composition $A_2Pt_6Al_{15}$(A = Y, Gd-Tm, Zr). *Z. Anorg. Alleg. Chem.* **2004**, *630*, 361–368. [CrossRef]
14. Latturner, S.E.; Kanatzidis, M.G. $Gd_{1.33}Pt_3(Al,Si)_8$ and $Gd_{0.67}Pt_2(Al,Si)_5$: Two Structures Containing a Disordered Gd/Al Layer Grown in Liquid Aluminum. *Inorg. Chem.* **2002**, *41*, 5479–5486. [CrossRef]
15. Murashova, E.V.; Tursina, A.I.; Bukhan'ko, N.G.; Gribanov, A.V.; Chernyshev, I.V.; Seropegin, Y.D. Ternary compounds $Ce_{0.67}Pt_2Al_5$ and $Ce_{1.33}Pt_3Al_8$. *J. Alloys Compd.* **2005**, *398*, 100–105. [CrossRef]
16. Lacerda, A.; Canfield, P.C.; Beyermann, W.P.; Hundley, M.F.; Thompson, J.D.; Sparn, G.; Fisk, Z.; Burns, C.; Barnhart, D.; Lawson, A.C.; et al. Possible heavy-fermion behavior and field-induced transitions in new R-Pt-Ga compounds. *J. Alloys Compd.* **1992**, *181*, 191–196. [CrossRef]
17. Deppe, M.; Hartmann, S.; Macovei, M.E.; Oeschler, N.; Nicklas, M.; Geibel, C. Investigation of $Yb_2Pt_6Al_{15}$ single crystals:heavy fermion system with a large local moment degeneracy. *New J. Phys.* **2008**, *10*, 093017. [CrossRef]
18. Matsumoto, Y.; Ueda, T.; Ohara, S. Single crystal growth and heat capacity measurements of triangular lattice $R_2Pt_6Ga_{15}$ (R = rare earth). *J. Phys. Conf. Ser.* **2016**, *683*, 012035. [CrossRef]
19. Kwei, G.H.; Lawson, A.C.; Larson, A.C.; Morosin, B.; Larson, E.M.; Canfield, P.C. Structure of $Ce_2Pt_6Ga_{15}$: Interplanar Disorder from the Ce_2Ga_3 Layers. *Acta Cryst.* **1996**, *B52*, 580–585. [CrossRef]
20. Yamashita,T.; Ohara, S. Non-Fermi liquid behavior on heavy-fermion system $Ce_2Pt_6Ga_{15}$. *J. Phys. Conf. Ser.* **2012**, *400*, 042074. [CrossRef]
21. Radzieowski, M.; Stegemann, F.; Block, T.; Stahl, J.; Johrendt, D.; Janka, O. Abrupt Europium Valence Change in $Eu_2Pt_6Al_{15}$ around 45 K. *J. Am. Chem. Soc.* **2018**, *140*, 8950–8957. [CrossRef]
22. Radzieowski, M.; Stegemann, F.; Hoffmann, R.-D.; Janka, O. The monoclinic superstructure of the $M_2Pt_6Al_{15}$ series (M = Ca, Sc, Y, La, Lu). *Z. Kristallogr.* **2017**, *232*, 2050.
23. Macaluso, R.T.; Shatruk, M.; Chai, P.; Hong, H.; Wangeline, C.; Ryan, K.; Holton, P.; Allaz, J.; Morrison, G.; Fulfer, B.; Fronczek, F.; Chan, J.Y. Synthesis, structure, and magnetic behavior of $(La_xCe_{1-x})_{1.33}Pt_4Ga_{10}$ ($0 \leq x \leq 1$). *J. Alloys Compd.* **2014**, *600*, 193–198. [CrossRef]
24. Nguyen, S.D.; Ryan, K.; Chai, P.; Shatruk, M.; Xin, Y.; Chapman, K.W.; Chupas, P.J.; Fronczek, F.R.; Macaluso, R.T. $Pr_{1.33}Pt_4Ga_{10}$: Superstructure and magnetism. *J. Solid State Chem.* **2014**, *220*, 9–16. [CrossRef]
25. Radzieowski, M.; Stegemann, F.; Janka, O. Magnetic Properties of the $RE_2Pt_6X_{15}$ (RE = Y, La–Nd, Sm, Gd–Lu; X = Al, Ga) Series. *Eur. J. Inorg. Chem.* **2020**, *2020*, 1199–1210. [CrossRef]
26. Zhuravleva, M.A.; Chen, X.Z.; Wang, X.; Schultz, A.J.; Ireland, J.; Kannewurf, C.K.; Kanatzidis, M.G. X-ray and Neutron Structure Determination and Magnetic Properties of New Quaternary Phases $RE_{0.67}Ni_2Ga_{5+n-x}Ge_x$ and $RE_{0.67}Ni_2Ga_{5+n-x}Si_x$ (n = 0, 1; RE = Y, Sm, Gd, Tb, Dy, Ho, Er, Tm) Synthesized in Liquid Ga. *Chem. Mater.* **2002**, *14*, 3066–3081. [CrossRef]
27. Kotur, B.Y.; Bruvo, M. Crystal structure of the silicide $Sc_{1.2}Fe_4Si_{9.8}$. *Sov. Phys. Crystallogr.* **1991**, *36*, 787–789.
28. Noguchi, S.; Okuda, K.; Adachi, T.; Yoshida, T. Synthesis and characterization of new ternary silicide $Er_{1.2}Fe_4Si_{9.8}$. *Physica B* **1997**, *237*, 612–615. [CrossRef]
29. Han, M.K.; Wu, Y.Q.; Kramer, M.; Vatoves, B.; Grandjean, F.; Long, G.J.; Miller, G.J. Superstructure in $RE_{2-x}Fe_4Si_{14-y}$ (RE = Y, Gd-Lu) Characterized by Diffraction, Electron Microscopy, and Mo1ssbauer Spectroscopy. *Inorg. Chem.* **2006**, *45*, 10503–10519. [CrossRef]
30. Manni, S.; Lin, Q.; Bud'ko, S.L.; Canfield, P.C. Systematic investigation of structural, transport, magnetic and thermodynamic properties of hexagonal $R_2Pt_6Al_{15}$ (R = Y, La-Nd, Sm-Lu) series. In Proceedings of the MAR16 Meeting of the American Physical Society, USA, 16 March 2015.

31. Suzuki, H.; Yamamoto, R.; Onimaru, T.; Urushihara, D.; Nakamura, S.; Ohara, S. Single crystal growth and physical properties of heavy fermion $Ce_2P_6Al_{15}$. In Proceedings of the the Autumn Meeting of the Japan Physical Society, Tokyo, Japan, 12 September 2022; 12pW541-10.
32. Izumi, F.; Momma, K.Three-Dimensional Visualization in Powder Diffraction. *Solid State Phenom.* **2007**, *130*, 15–20. [CrossRef]
33. Sheldrick, G.M. A short history of SHELX. *Acta Cryst. A* **2008**, *64*, 112–122. [CrossRef] [PubMed]
34. Ravel, B.; Newville, M. ATHENA, ARTEMIS, HEPHAESTUS: Data analysis for X-ray absorption spectroscopy using IFEFFIT. *J. Synchrotron Radiat.* **2005**, *12*, 537–541. [CrossRef] [PubMed]
35. Tursina, A.I.; Murashova, E.V.; Noël, H.; Bukhan'ko, N.G.; Seropegin, Y.D. Crystal structure and magnetic properties of the new intermetallic $Ce_2Pt_9Al_{16}$. *Intermetallics* **2009**, *17*, 780–783. [CrossRef]
36. Strydom, A.M. The Cage Compound $Ce_2Pt_9Al_{16}$: A Low-Temperature Magnetic Field Study. *J. Low. Temp. Phys.* **2013**, *170*, 334–339. [CrossRef]
37. Haen, P.; Flouquet, J.; Lapierre, F.; Lejay, P.; Remenyi, G. Metamagnetic-Like Transition in $CeRu_2Si_2$? *J. Low Temp.* **1987**, *67*, 391–419. [CrossRef]
38. Matsumoto, Y.; Hanya, K.; Haga, Y.; Fisk, Z.; Ohara, S. Single crystal growth and physical properties of $YbPd_2Si_2$. *J. Phys. Conf. Ser.* **2015**, *592*, 012022. [CrossRef]
39. Bonville, P.; Hammann, J.; Hodges, J.A.; Imbert, P.; Jéhanno, G.; Besnus, M.J.; Meyer, A. Hybridisation and crystal field in $YbPd_2Si_2$. *Z. Phys. B* **1991**, *82*, 267–274. [CrossRef]